COLLAPSE RISK EVALUATION OF SELF-CENTERING STEEL MRFS WITH VISCOUS DAMPERS IN NEAR-FAULT REGIONS

George S. Kamaris[1], Angelos S. Tzimas[1], Theodore L. Karavasilis[1], and Carmine Galasso[2]

[1] School of Engineering, University of Warwick
Coventry CV4 7AL, United Kingdom
{G.Kamaris,A.Tzimas,T.Karavasilis}@warwick.ac.uk

[2] Department of Civil, Environmental and Geomatic Engineering and Institute for Risk and Disaster Reduction, University College London (UCL)
London WC1E 6BT, United Kingdom
c.galasso@ucl.ac.uk

Keywords: Self-centering, Steel frames, Dampers, Collapse Risk, Near-fault, Hazard analysis.

Abstract. *This paper presents an evaluation of the seismic collapse risk of self-centering moment-resisting frames (SC-MRFs) with viscous dampers located in near-fault regions. This evaluation is based on the comparison of different designs of a prototype steel building using four lateral load resisting frames: 1) conventional moment-resisting frames (MRFs), 2) MRFs with viscous dampers, 3) SC-MRFs and 4) steel SC-MRFs with viscous dampers. The frames are modeled in OpenSees where material and geometrical nonlinearities are taken into account as well as cyclic strength and stiffness degradation. A database of 91 near-fault, pulse-like ground motions with varying pulse periods is employed for the nonlinear dynamic analyses. Collapse resistance of the frames is evaluated through incremental dynamic analysis (IDA). The results of the IDA are combined with probabilistic seismic hazard analysis models that account for near-fault directivity to assess collapse risk of the structures. Results show that the predicted collapse capacity is affected by the pulse period of the near-fault ground motions and highlight that self-centering connections can significantly improve the collapse resistance of conventional MRFs. Finally, it is shown that supplemental damping provides superior collapse resistance for all frames.*

1 INTRODUCTION

A distinct velocity pulse with a long period often characterizes near-fault earthquake ground motions. Such pulse is typically observed at the beginning of the fault-normal (FN) ground velocity time-history and has a probability of occurrence that depends on the site-to-source geometry, earthquake magnitude and other parameters [1-2]. Starting from the pioneer studies of Veletsos and Newmark [3] and Bertero et al. [4], the response of yielding single-degree-of-freedom systems subjected to near-fault earthquake ground motions has been extensively studied by many researchers [5-6 and references therein]. Other studies focused on yielding frames and showed the potential of near-fault ground motions to induce large story drifts [7-9 and reference therein].

The destructive potential of near-fault ground motions was evident after many earthquakes such as the Northridge, California (1994); Kobe, Japan (1995); Chi-Chi, Taiwan (1999); and L'Aquila, Italy (2009). The economic losses caused by these earthquakes at near-fault sites highlighted the limitations of conventional seismic-resistant systems, which experience significant inelastic deformations (i.e. damage) in main structural members and appreciable residual story drifts.

Modern codes in the USA have adopted risk-targeted seismic design maps, which define design spectral acceleration values that are intended to ensure that newly designed buildings have a uniform probability of collapse of 1% in 50 years [10]. However, in their current form, they do not explicitly account for the higher potential collapse risk for buildings located in the near-fault region. A recent study highlighted the need to account for such higher collapse risk by showing that the probability of collapse in 50 years for reinforced concrete buildings at a representative near-fault site is approximately 6%, i.e. significantly higher than the 1% limit [11].

The issue of large residual story drifts and higher collapse risk in the near-fault region could be possibly addressed by employing modern resilient structures instead of the conventional yielding structures, which are promoted by current seismic codes such as the Eurocode 8 (EC8) [12]. Steel self-centering moment-resisting frames (SC-MRFs) using post-tensioned (PT) beam-column connections are a promising class of resilient structures. SC-MRFs exhibit softening force-drift behavior and eliminate beam inelastic deformations and residual drifts (RDs) as the result of gap opening developed in beam-column interfaces and elastic PT bars which clamp beams to the columns and provide self-centering capability. PT connections use yielding-based [13-19] or friction-based [20-23] energy dissipation devices, which are activated when gaps open and can be easily replaced if damaged. Seismic design procedures for SC-MRFs have been proposed in [24-25]. Steel moment-resisting frames (MRFs) equipped with passive dampers are another class of resilient structures. Previous analytical and experimental research showed that steel MRFs with passive dampers can be designed to be lighter and perform better than conventional steel MRFs under the design basis earthquake (DBE) and the maximum considered earthquake (MCE) [26-27]. A study shows that supplemental viscous damping does not always ensure adequate reduction of RDs [26-28]. A recent work evaluates the seismic collapse resistance of steel MRFs with linear viscous dampers and shows that supplemental viscous damping does not always guarantee a better seismic collapse resistance when the strength of the steel MRF with dampers is lower or equal to 75% of the strength of a conventional steel MRF [29].

Recent studies investigated the effectiveness of a seismic design strategy that combines self-centering systems with viscous dampers. The use of viscous dampers in parallel to self-centering precast concrete base rocking walls has been proposed as an effective way to control peak story drifts [30]. The parallel combination of hysteretic and viscous energy dissipa-

tion along with a friction slip mechanism in series connected to the viscous energy dissipation mechanism were found to achieve high levels of seismic performance for self-centering systems [31]. Tzimas et al. [32] also proposed a new seismic design procedure for SC-MRFs equipped with viscous dampers in the framework of EC8 [12].

Although the response of resilient structures has been thoroughly investigated up to the MCE, research on their behavior near collapse is still missing. In addition, their collapse risk in the near-source has not been studied. In this paper, the seismic collapse risk of SC-MRFs with viscous dampers subjected to near-fault ground motions is evaluated and compared to that of ordinary MRFs. The recently developed PT connection with web hourglass shape pins (WHPs) [15,18] is utilized for the SC-MRFs. A prototype building is designed as a SC-MRF with or without viscous dampers. Different design approaches for the SC-MRF with viscous dampers are considered to investigate all possible scenarios. The structures are modeled in OpenSees [33] where material and geometrical nonlinearities are taken into account as well as cyclic strength and stiffness degradation. A database of 91 near-fault, pulse-like ground motions with varying pulse periods is employed for the nonlinear dynamic analyses of this study. The concept of incremental dynamic analysis (IDA) [34] is used for the prediction of collapse, in which each ground motion is scaled appropriately, using as intensity measure the first-mode spectral acceleration, $S_a(T_1)$, until dynamic instability occurs. The probability of collapse is then calculated as a function of ground motion characteristics i.e. the ground motion intensity and the period of the velocity pulse. Finally, the results of the IDA are combined with probabilistic seismic hazard analysis models that account for near-fault directivity to assess collapse risk of the structures.

2 SC-MRFS WITH VISCOUS DAMPERS

2.1 *SC-MRFs using PT connections with WHPs*

Figure 1(a) shows a SC-MRF using PT connections with WHPs and Figure 1(b) shows an exterior PT connection with WHPs. The PT connection with WHPs has been experimentally and numerically evaluated by Vasdravellis et al. [15,18]. Two high strength steel bars located at the mid depth of the beam, one at each side of the beam web, pass through holes drilled on the column flanges. The bars are post-tensioned and anchored to the exterior columns. WHPs are inserted in aligned holes on the beam web and on supporting plates welded to the column flanges. Energy is dissipated through inelastic bending of the WHPs that have an optimized hourglass shape (Figure 1(c)) with enhanced fracture capacity. The beam web and flanges are reinforced with steel plates. The panel zone is strengthened with doubler and continuity plates. A fin plate welded on the column flange and bolted on the beam web is used for easy erection and resistance against gravity loads before post-tensioning. Slotted holes on the beam web ensure negligible influence of the fin plate on the PT connection hysteretic behavior.

The connection behavior is characterized by gap opening and closing in the beam-column interface as a result of the re-centering force in the PT bars. Figure 2(a) shows the free body diagram of an external PT connection where d_{1u} and d_{1l} are the distances of the upper and lower WHPs from the center of rotation that is assumed to be at the inner edge of the beam flange reinforcing plates; d_2 is the distance of the PT bars from the center of rotation; T is the total force in both PT bars; $F_{WHP,u}$ and $F_{WHP,l}$ are the forces in the upper and lower WHPs; C_F is the compressive force in the beam-column interface; V_{C1u} and V_{C1l} are the shear forces in the upper and lower column, M is the PT connection moment, V is the beam shear force; and N is the horizontal clamping force that is transferred to the beam-column interface through the slab diaphragm and the beam. Figure 2(b) shows the SC-MRF expansion due to rotations θ in the PT connections.

(a)

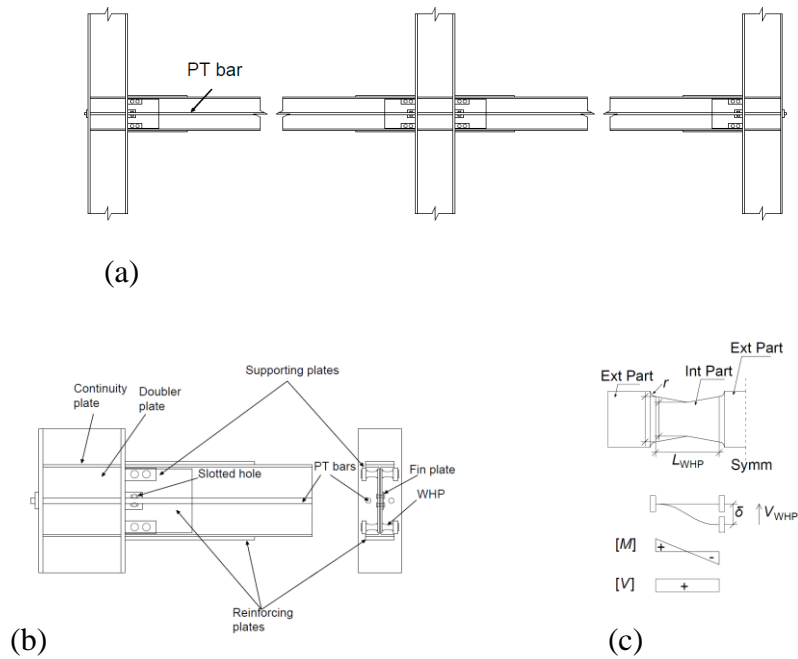(b)   (c)

Figure 1: (a) SC-MRF; (b) exterior PT connection with WHPs; and (c) WHP geometry and assumed static system.

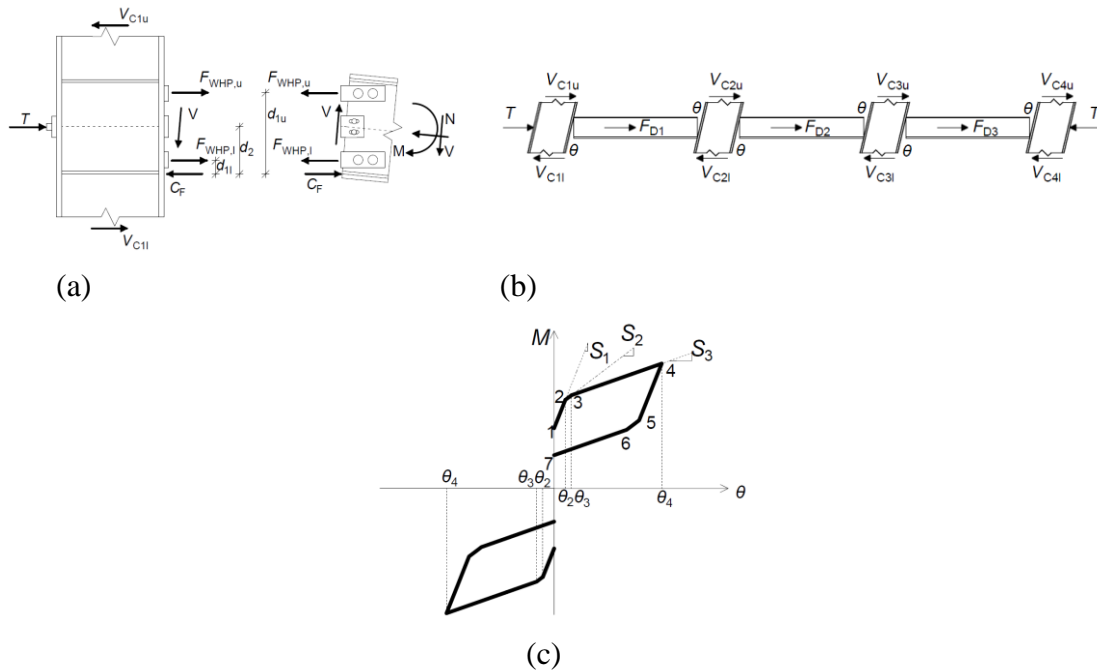(a)   (b)

(c)

Figure 2: (a) Free body diagram of an external PT connection; (b) SC-MRF expansion and horizontal forces equilibrium; and (c) theoretical cyclic behaviour of the PT connections with WHPs.

Figure 2(c) shows the theoretical cyclic moment-rotation (M-θ) behavior of the PT connection with WHPs, which has been verified by the large-scale experiments conducted by Vasdravellis et al. [15]. After decompression of the PT connection (Point 1 in Figure 2(c)), gap opens and the behavior becomes nonlinear elastic with rotational stiffness S_1. At point 2, the upper WHPs yield and M continues to increase with slope S_2. At point 3, the lower WHPs

yield and M continues to increase with slope S_3. When loading is reversed, the connection begins to unload until the gap closes. More details about the connection behavior can be found in [32].

2.2 Prototype building

Figure 3(a) shows the plan view of a 5-storey, 5-bay by 3-bay prototype building having two identical lateral resisting frames (MRFs or SC-MRFs) in the x plan direction. Braced frames are located in the y plan direction. Viscous dampers are inserted in the interior gravity frames, with pinned connections, that are coupled with the perimeter lateral resisting frames through the floor diaphragm as shown in Figure 3(b). Due to the symmetry of the building, this paper focuses on one perimeter lateral resisting frame. The building has ductile non-structural elements, and thus, maximum interstory drift ratio $\theta_{s,max}$, should be lower than 0.75% under the under the frequently occurred earthquake (FOE) according to EC8 [12]. The DBE is expressed by the Type 1 elastic response spectrum of EC8 [12] with peak ground acceleration equal to 0.35g and ground type B. The FOE has intensity of 40% the intensity of the DBE. The model used for the design is based on the centerline dimensions of the lateral resisting frame without accounting for the finite panel zone dimensions. A "lean-on" column is included in the model to account for the P-Δ effects of the vertical loads acting on the gravity columns in the tributary plan area (half of the total plan area) assigned to the lateral resisting frame. The steel yield strength is equal to 355 MPa for the columns, 275 MPa for the beams, 930 MPa for PT bars, 235 MPa for the WHPs, 275 MPa for the beam reinforcing plates and 235 MPa for the fuse. The beam and column sections have different steel grades to achieve the capacity design rules of EC8 [12]. Nonlinear viscous dampers are designed with a horizontal configuration and a velocity exponent a equal to 0.5. The inherent damping ratio of the SC-MRF is equal to 3%.
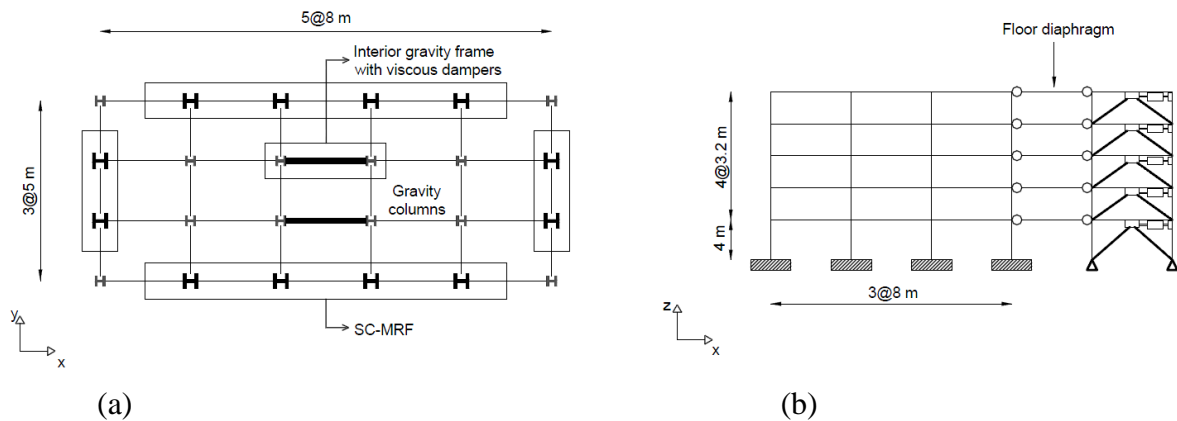

Figure 3: (a) Plan and (b) side views of the prototype building.

2.3 Design cases

Four frames were designed as SC-MRFs with and without viscous dampers and conventional MRFs with and without viscous dampers. All the frames have the same cross sections, but different structural performance under strong earthquakes. Table 1 provides the steel weight, fundamental period T_1, damping ratio ξ_t and interstory drift ratio, $\theta_{s,max}$, under the FOE and DBE of the frames discussed below:

CP3D (SC-MRF or MRF): Conventional performance frame without viscous dampers (ξ_t =3%).

HP20D (SC-MRF or MRF): High performance frame with viscous dampers (ξ_t =20%). Its target performance led to the same cross sections and PT connections details with those of *CP3D* frame. It demonstrates the design scenario where viscous dampers are used to achieve $\theta_{s,max}$ significantly lower than the EC8 [12] limit. It also demonstrates the design scenario where strict design criteria for the PT connections along with a low $\theta_{s,max}$ target value are enforced to genuinely achieve seismic resilience.

Table 2 provides the beams and columns cross-sections and the damping coefficient of the dampers, c, of the frames. The PT bar diameter, d_{PT}, the total initial post-tensioning force, T_0, the length, L_{rp}, the area, A_{rp}, of the beam flange reinforcing plate, the length of half a WHP, L_{WHP} (Figure 1(c)), the external, D_e, and internal, D_i, diameters of the WHPs of the SC-MRFs are also listed in this table.

FRAME	Steel weight[*] (kN)	T (s)	ξ_t (%)	$\theta_{s,max}$ FOE (%)	$\theta_{s,max}$ DBE (%)
CP3D SC-MRF	268	1.27	3.00	0.72	1.80
HP20 SC-MRF	268	1.27	20.0	0.48	1.20
CP3D MRF	268	1.27	3.00	0.72	1.80
HP20D MRF	268	1.27	20.0	0.48	1.20

[*]Beams and columns

Table 1: Data and design criteria for the frames with and without viscous dampers.

Storey	Cross sections			PT bars		WHPs			Reinforcing plates		Viscous dampers c (kN·(s./m)^0.5)	
	Beams	Columns	Gravity columns	T_0 (kN)	d_{PT} (mm)	D_e (mm)	D_i (mm)	L_{WHP} (mm)	L_{rp} (mm)	A_{rp} (mm)	CP3D	HP20D
1	IPE550	HEB650	HEB240	1087	50	43	33	70	1392	7350	-	2139
2	IPE600	HEB650	HEB240	1256	60	46	36	70	1660	10120	-	1641
3	IPE550	HEB650	HEB240	1087	48	43	33	70	1416	7350	-	1416
4	IPE500	HEB600	HEB220	941	38	41	30	70	1092	5200	-	1102
5	IPE500	HEB600	HEB220	941	36	39	28	70	743	4400	-	810

Table 2: Design details for the CP3D and the HP20D frames.

3 NONLINEAR MODELS

Models for the SC-MRFs are developed in OpenSees [33]. The columns and the reinforced lengths of the beams are modeled as nonlinear force-based beam-column fiber elements. Fibers have bilinear elastoplastic stress-strain behavior (Steel01 [33]) with post-yield stiffness ratio equal to 0.003.

Beam local buckling is expected after the end of the reinforcing plates, and so, the unreinforced lengths of the beams are modeled as elastic elements with zero length nonlinear fiber hinges at their ends that exhibit strength and stiffness deterioration [35]. The fiber hinge sections are composed of the *Bilin* material [33] that simulates the modified Ibarra–Krawinkler [35] deterioration model. The hinges are calibrated individually in order to exhibit the same behavior as the multi-linear deteriorating concentrated hysteresis model [36].

For the PT connection, a simplified model is adopted [37] where the *M-θ* behavior of the PT connection is simulated by inserting 2 rotational springs in parallel at the beams ends. The

first spring corresponds to the PT bars behavior, while the second one corresponds to the behavior of the WHPs. The PT bars behavior is modeled using a bilinear elastic model, while for the modeling of the WHPs, a smooth bilinear elastoplastic model is used.

Panel zones are modeled using the Krawinkler model [38] which consists of four rigid links connected at the corners by rotational springs. The springs at the lower left and upper right corners have no stiffness, and thereby act as true hinges. The spring at the upper left is used to represent panel zone shear resistance, and the spring at the lower right is used to represent column flange bending resistance.

To account for P-Δ effects, the gravity columns associated with one of the two lateral resisting frames of the plan in Figure 3(a) are modeled as 3 lean-on columns, i.e. one for each bay of the frame. Diaphragm action is modeled with truss elements connecting the lean-on columns nodes to nodes defined along the length of the beams at the points where secondary beams are placed. These trusses have stiffness of 100 times the axial beam stiffness.

Nonlinear viscous dampers are modeled with zero length elements (Viscous material [33]), while their supporting braces are modeled with elastic braces as they are strong enough to avoid buckling. In the analytical model, the damper limit states caused by their stroke limit are not considered, i.e. it is assumed that dampers will be manufactured with enough stroke to avoid reaching their limit states even under very large storey drifts.

The connections of the conventional MRFs are assumed to be rigid and have full strength, while beams are modeled as elastic elements with zero length rotational springs at their ends that exhibit strength and stiffness deterioration [35]. Columns and panel zones are modeled as described above for the SC-MRFs.

The OpenSees models for the SC-MRFs and the conventional MRFs include the effect of the panel zone stiffness, and so, result in T value shorter than 1.27 s that is based on the centerline models used for design. T from the OpenSees [35] models is 0.94 s for *CP3D* and *HP20D* SC-MRFs and 1.18 s for *CP3D* and *HP20D* MRFs.

4 GROUND MOTIONS CONSIDERED

A set of 91 pulse-like ground motions is used in 2D nonlinear dynamic time history analyses of the abovementioned SC-MRFs and MRFs. These ground motions were selected by Baker [39] from the PEER NGA [40] database by implementing wavelet analysis for the detection of pulses. A wavelets-based algorithm was used, which assigns a score, a real number between 0 and 1, to each record and determines the pulse period, T_p. The larger the score the more likely the record is to show a pulse. Only the FN ground motions having a pulse score equal or larger than 0.85 and a minimum peak ground velocity of 30cm/s were, arbitrarily, counted as pulse-type records.

Ground motions were recorded from earthquakes with moment magnitudes, M, varying from 5.0 to 7.6 and include pulse periods that vary between 0.4 and 12.9 s. Although all of the records exhibit velocity pulses, site-to-source distances were not considered in the selection criteria and range from 0.10 to 102 km. Thus, some of the observed pulses were probably caused by other geological mechanisms, such as basins. Nevertheless, all pulse-like records are taken as representative of near-fault ground motions, assuming that large velocity pulses will produce similar structural response regardless of their geological characteristics. All of the records in the database have been rotated to the fault-normal direction. A complete list of the pulse-like ground motions used in this study can be found in [39].

In this study, the collapse seismic risk of the structures depends on the probability of occurrence or not of a pulse-like ground motion, which is calculated through the theorem of total probability. For this reason, a second set of far-field records is needed for the determination of collapse probability for sites that are not influenced by forward directivity

effects. Similarly to [11], the set of far-field ground motions used in this study is based on the FEMA P695 [41] far-field ground motion set, which includes 22 record pairs, each with two horizontal components for a total of 44 ground motions. Those ground motions are recorded at sites located greater than or equal to 10 km from fault rupture; event magnitudes range from *M* 6.5 to *M* 7.6 with an average magnitude of *M* 7.0. According to the NEHRP Site Class, 16 sites are classified as Site Class D (stiff soil sites) and the remaining are classified as Site Class C (very stiff soil sites). The wavelet classification algorithm developed by Baker [40] indicates that nine of these ground motion records have pulses in the velocity history [11]; these pulse-like record were then removed from the far-field database. It is worth noting that the ground motion records were selected without consideration of spectral shape. In fact, the FEMA P695 [41] far-field ground motion set consists of records that are structure type and site hazard independent, i.e., records do not depend on period, or other building-specific properties of the structure, as well as on hazard disaggregation, or other site- or hazard- dependent properties.

5   COLLAPSE EVALUATION

The collapse seismic intensity of each frame is assessed through IDA [34]. According to this methodology, the frame model is subjected to a specific ground motion scaled to multiple levels of intensity, until collapse occurs, as indicated by the dynamic instability of the structural system. For each intensity level a response parameter of the structure (e.g., story displacements, floor accelerations, etc.) is monitored to produce an IDA curve. This process is repeated for all earthquake records and for each frame. In this work, the spectral acceleration at the fundamental period T_1 of each building, $S_a(T_1)$, is used as intensity measure and the interstory drift ratio is the response parameter that is monitored. To determine the limit of total loss of lateral resistance, the incremental slopes are calculated by drawing straight lines between the consecutive data points in the IDA curve. The lowest S_a value corresponding to the ith data point with the slope between the ith and i+1th points being less than 10% of the initial slope on the IDA curve is defined as the collapse capacity of the frames in this study, where the initial slope is determined from the straight line from the origin of axis to the first data point of the IDA curve. The IDA curves for the *HP20D* SC-MRF, obtained for the ensemble of the far-fault ground motions, are shown in Figure 4(a).

The collapse capacities obtained from the IDA curves are used for the construction of a fragility curve for each frame. Fragility curves express the probability of collapse due to earthquakes as a function of ground motion intensity. They are usually assumed to have the form of a lognormal cumulative distribution function with a median value, θ, and logarithmic standard deviation, β, of the ground motion intensities at which collapse occurs in IDA. The fragility curve resulted for the *HP20D* SC-MRF is shown in Figure 4(b) with a solid line together with the results from the numerical analyses.

The parameter β influences the shape of the fragility curve and reflects the level of uncertainty in the analysis results. Figure 4(b) shows two fragility curves corresponding to two different values of β. The solid curve has a value of $\beta_{RTR}=0.35$ and the dashed curve reflects a $\beta_{Total}=0.80$. As indicated in this figure, larger values of β have the effect of "flattering" the curve. Two sources of uncertainty in quantifying the collapse capacity of structural systems are considered herein: aleatory sources and epistemic. The aleatory or record-to-record uncertainty, reflects the variability in the response of the structures due to the random nature of ground motions. The epistemic or modeling uncertainty is mainly due to lack of knowledge about the building's real model and real element properties. It is associated with nonlinear modeling, based on the evaluation of the accuracy and robustness of the nonlinear models

used and their ability to represent the true physical properties and the seismic response of structures.
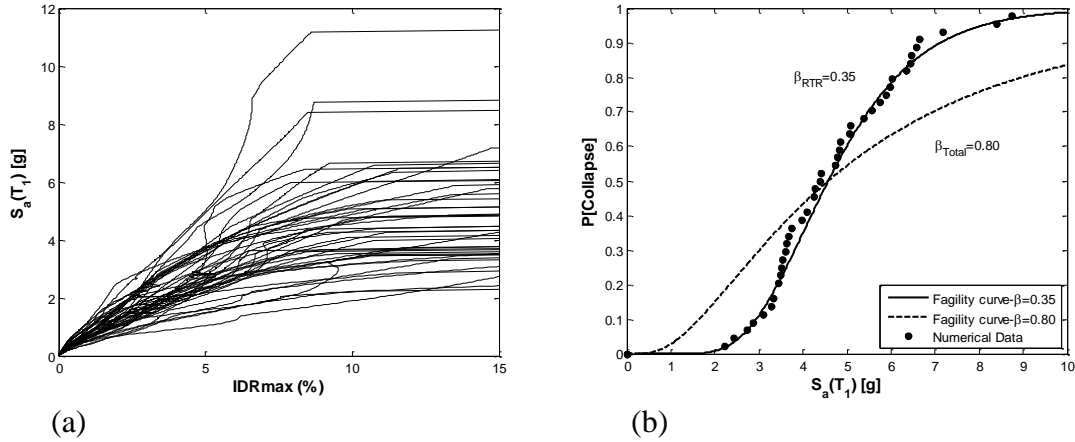

Figure 4: (a) IDA curves for the *HP20D* SC-MRF (b) Corresponding fragility curve.

In order to combine the contributions of aleatory and epistemic uncertainties, the mean estimates approach is used herein [42]. When the record-to-record uncertainties are only considered, the structural response is well-described by a lognormal distribution, with a median, θ, and standard deviation, β_{RTR}. In addition, it is assumed that the epistemic uncertainty is also lognormally distributed with a median, θ, and standard deviation, $\beta_{modeling}$, and that the random variables associated with these two uncertainties are statistically independent. Consequently, when these two distributions are combined the resulting distribution is also lognormal with a median, θ, and a standard deviation given by the following equation:

$$\beta_{Total} = \sqrt{\beta_{RTR}^2 + \beta_{modeling}^2}$$ (1)

Thus, when the mean estimates approach is used, the median is unchanged when modeling uncertainties are incorporated, but the standard deviation increases. Values of β_{Total} are taken as 0.80, β_{RTR} is calculated based on the IDA results and the $\beta_{modeling}$ is derived though Equation (1). This value of β_{Total} has been adopted by other researchers [11] and seems to be logical for the risk assessment of frame systems. Note that the fragility curves, as shown in Figure 4(b), have not yet been adjusted to account for the distinct spectral shape of rare ground motions, characterized by the parameter ε [43]. To do so, the methodology proposed by Haselton et al. [44] was employed.

The risk assessment procedure of the frames, when subjected to near fault ground motions, is modified properly to take into account the effect of the pulse period of the record, T_p, and is based on the approach proposed by Champion and Liel [11]. This methodology is described in the following sections.

6 EFFECT OF PULSE PERIOD IN COLLAPSE ASSESSMENT

The pulse period, T_p, of the near-field ground motions strongly affects seismic collapse capacity of structures. To show this effect in the frames studied herein, the collapse capacities of the *HP20D* SC-MRF obtained from IDA curves are plotted versus the ratio T_p/T_1 and are shown in Figure 5 as individual points.

In addition, the moving average of the numerical data is computed by averaging the point of interest with the five previous and subsequent data points. This is done to fit the data points with a trend-line in order to investigate the behavior of collapse capacity. The shape of the

moving average curve illustrates the influence of the pulse period to collapse capacity. The maximum values of collapse capacities are obtained in the region of the moving average curve where the fundamental period of the frame is approximately equal to the T_p of the record, i.e. $T_p/T_1 \approx 1$. This result is not consistent with the response of structures in the elastic range, since the largest displacement demand of these systems is observed when the period of the excitation is very close to T_1. In contrary, collapse of structures is a very nonlinear phenomenon, which is characterized by large inelastic deformations due to severe damage induced to the structure. For this reason, the stiffness of the structure decreases, resulting in a significant elongation of its effective period. Therefore, collapse capacity is larger in this region, because it is influenced by the real elongated period of the building which is different than the elastic one. In addition, ground motions with longer pulse period are the most damaging, giving very low collapse resistances. This is attributed to the effective lengthened period of the structure which tends to coincide with the pulse period of the excitation. In the region of $T_p < T_1$ the collapse capacity of the frame tends to decrease, and this is probably due to high spectral velocities exhibiting in the shortest pulse period records.
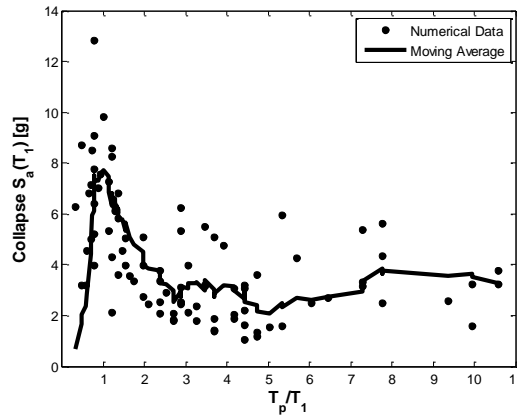

Figure 5: Collapse capacities of the *HP20D* SC-MRF versus the T_p/T_1 ratio together with the generated moving average curve.

7 COLLAPSE FRAGILITY FUNCTIONS INCLUDING NEAR-FAULT DIRECTIVITY

Near-fault directivity has an impact in collapse capacity of the structures, so it should be taken into account in their risk assessment. Collapse of structures depends not only on $S_a(T_1)$, but also whether a ground motion record exhibits a velocity pulse and the corresponding pulse period (see Figure 5). To incorporate this effect in the collapse fragility functions, the theorem of total probability is utilized to calculate the probability of collapse, $P[Col/S_a = x]$, given a specific value of $S_a(T_1)$, i.e. the fragility function of each frame [11]:

$$P[Col \,|\, S_a = x] = P[Col \,|\, S_a = x, Pulse] \cdot P[Pulse \,|\, S_a = x] + P[Col \,|\, S_a = x, NoPulse] \cdot P[NoPulse \,|\, S_a = x] \,(2)$$

where $P[Col/S_a = x, Pulse]$, $P[Col/S_a = x, No\ Pulse]$, $P[Pulse/S_a = x]$ and $P[No\ Pulse/S_a = x]$ are the probability of collapse for pulse like ground motions, the probability of collapse for far-fault ground motions, the probability that a ground motion record exhibits a velocity pulse and the probability that a ground motion record does not exhibit a velocity pulse, respectively.

The term $P[Col/S_a = x, No\ Pulse]$ is determined from the fragility curves, obtained from the IDA results for the far-fault ground motions. The collapse probability when a pulse occurs, $P[Col/S_a = x, Pulse]$, depends on the pulse period and the likelihood of different pulse periods occurring, $P[T_p = t_i | S_a = x, Pulse]$:

$$P[Col \mid S_a = x, Pulse] = \sum_{i=1}^{All \; T_p} P[Col \mid T_p = t_i, S_a = x, Pulse] \cdot P[T_p = t_i \mid S_a = x, Pulse] \quad (3)$$

The probability of collapse for a given pulse period T_p value, $P[Col/T_p=t_i, S_a=x, Pulse]$, is computed through the moving average curve constructed for each frame. The moving average represents the median collapse capacity as a function of T_p. For any value of T_p and $S_a(T_1)$, the probability of collapse is computed by assuming a lognormal distribution with a median equal to the value of $S_a(T_1)$ of the moving average curve for a given T_p and a standard deviation $\beta_{Total} = 0.8$.

The remaining parts of Equations (2) and (3) are computed with the aid of probabilistic seismic hazard analysis (PSHA), which provides the mean annual frequency, λ, of exceeding an IM level, x. Conventional far-field PSHA gives λ according to the following equation:

$$\lambda_{IM>x} = \sum_{i=1}^{N} v_i \int_m \int_r P[IM > x \mid m,r] f_{M,R}(m,r) dm dr \quad (4)$$

where v_i is the mean annual rate of earthquakes occurrence on a nearby fault i, N is the total number of faults, M is the moment magnitude, R is the source-to-site distance and $f_{M,R}$ is the joint probability density function of M and R. The expression $P[IM > x/m, r]$ is the probability that the ground motion intensity exceeds a specific value, x, given an earthquake of magnitude m at distance r, which can be obtained from ground motion prediction equations (GMPEs). Different IM are used in these equations (in this work $S_a(T_1)$ is adopted).

PSHA has been recently modified to account for near source conditions, i.e., Near-source Probabilistic Seismic Hazard Analysis (NS-PSHA); more details, including implementation and applications, can be found in [2,45-49]. According to this methodology, Equation (4) is adjusted to account for potential near-source directivity by an additional term, Z, which defines the site-to-source geometry:

$$\lambda_{IM>x} = \sum_{i=1}^{N} v_i \int_m \int_r \int_z P[IM > x \mid m,r,z] f_{M,R,Z}(m,r,z) dm dr dz \quad (5)$$

In this case the probability that a specific ground motion intensity value is exceeded, $P[IM > x/m, r, z]$, depends on the probability of occurrence of a pulse, the distribution of possible pulse periods and the peculiar spectral shape induced by the pulse. The probability of a pulse occurring is a function of site-to-source geometry and decreases with distance from the fault and for shorter fault rupture lengths [2,46]. The pulse period distribution is a function of earthquake magnitude, with larger magnitude events usually causing longer pulse periods [46,50].

When the NS-PSHA has been conducted for a given IM level, the probability that a pulse occurs, $P[Pulse/S_a = x]$, can be calculated by the following equation:

$$P[Pulse \mid S_a = x] = \frac{\lambda_{S_a=x,Pulse}}{\lambda_{S_a=x,Total}} \quad (6)$$

where $\lambda_{Sa=x,Pulse}$ is the mean annual frequency of $S_a = x$ when only pulse-like ground motions are considered and $\lambda_{Sa=x,Total}$ is the mean annual frequency of $S_a = x$ when both pulse-like and far-fault ground motions occur. Note that NS-PSHA is computed here as $\lambda_{Sa=x}$ rather than $\lambda_{Sa>x}$ to allow for combination with the collapse fragility curves. The hazard disaggregation of Eq. (6) is required for each spectral acceleration level of interest (from the collapse fragility); a similar disaggregation process can also be used to identify the contribution of each pulse

period, t_i, to each spectral value, i.e., $P[T_p = t_1|S_a = x, Pulse]$. Finally, the term $P[No\ Pulse/S_a = x]$ is derived through the following equation:

$$P[NoPulse\,|\,S_a = x] = 1 - P[Pulse\,|\,S_a = x] \tag{7}$$

As an example, a fixed (characteristic) M 7 strike-slip (SS) fault is considered here to compare the seismic performances of the structural systems introduced earlier. The single fault is 42km long based on the median Wells and Coppersmith magnitude-scaling relation [51] and is assumed to have a recurrence rate of 0.05 earthquakes per year. The location of earthquake epicenters is uniformly distributed along the fault while six sites with site-to-source distances equal to 5, 10 and 15 km at the end ("End-of-Fault" sites) and midpoint ("Midfault" sites) of the fault line are considered in this study (Figure 6(a)).
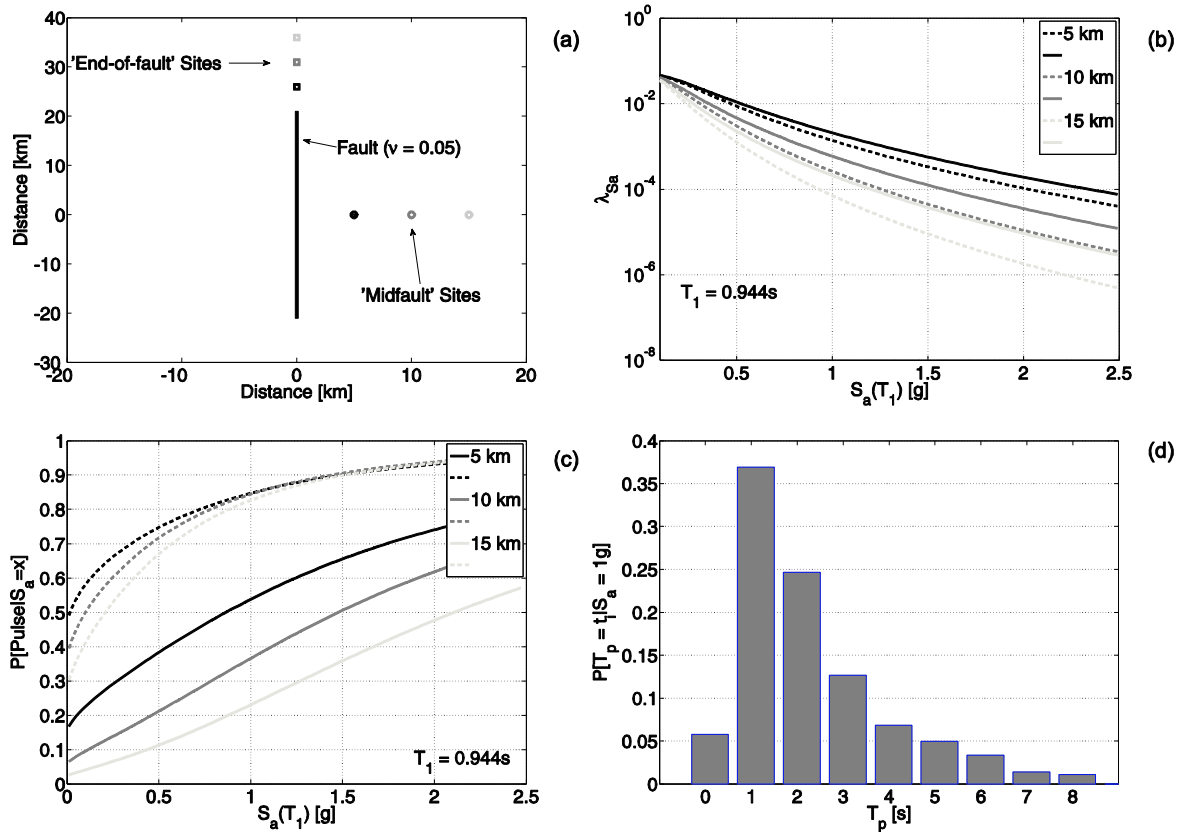

Figure 6: Representative near-field sites considered in this study, showing (a) site location and (b) seismic hazard curves for the midfault (dashed lines) and end-of-fault (solid lines) sites with varying site-to-source distances. Hazard disaggregation results show (c) the probability of pulse occurrence for the different sites at $S_a(T_1 = 0.944$ s) and (d) a typical pulse period distribution for one hazard level, $S_a(T_1) = 1$ g, at the 5 km midfault site.

The probability of a pulse occurring is computed by using the model in [2] and depends, in the case of a SS rupture, on rupture-to-site distance, R, the distance from the epicenter to the site measured along the rupture direction, s, and angle between the fault strike and the path from the epicenter to the site, θ (a similar model is introduced in [46]). As noted in [49], a deterministic relationship between these parameters and rupture length, position of the rupture on the fault and epicenter location exist, allowing to easily simulate the uncertainty involved for the hazard computations. However, while rupture length and rupture position are, in principle, random variables, the application here is implemented in the simplifying hypothesis of fixed rupture and position, similarly to the applications in [49]. Such a hypothesis appears to be acceptable if a single magnitude can be generated by the considered fault, as assumed in

this study where the main focus is to compare the seismic performances of different structural systems rather than to investigate NS-PSHA.

Finally, the pulse period prediction is based on the empirical model in [47], although others are available (e.g., [46]). More details for the NS-PSHA calculation used here, including the GMPE modification to account for the 'bump' of spectral ordinates around the pulse period, can be found in [48].

NS-PSHA results are illustrated in Figure 6(b) for $T_1 = 0.944$ s. Figures 6(c) and (d) provide disaggregated hazard results in terms of $P[Pulse/S_a = x]$ and $P[T_p = t_i|S_a = x, Pulse]$ respectively (the latter refer to $S_a = 1$ g as an example).

8   SEISMIC COLLAPSE RISK ASSESSMENT IN THE NEAR-SOURCE

Using the methodology of the previous section, the collapse fragility curves of all frames at the midfault sites for a distance 15 km away from the fault, are constructed and depicted in Figure 7(a). The fragility curves of the frames suggest that the least susceptible structures to collapse are the frames equipped with viscous dampers, with the *HP20D* SC-MRF exhibiting the lowest probabilities of collapse. Figure 7(b) shows the fragility curves obtained for the *HP20D* SC-MRF located at the midfault sites for site-to-source distances equal to 5, 10 and 15 km. It observed that the probability of collapse is reduced with distance from the fault, because the likelihood that a pulse occurs, $P[Pulse/S_a = x]$, decreases with distance and that affects the first part of Equation (2).

In addition, the probability of collapse in 50 years of the four frames is calculated at the midfault and end-of-fault sites, for site-to-source distances equal to 5, 10 and 15 km. To do so, a Poisson distribution of the earthquake occurrences is utilized, which is given by the following equation:

$$P[Collapse\ in\ 50\ years] = 1 - e^{-vt} \tag{8}$$

where t is the time in years and v is the mean annual frequency of collapse, computed by integrating the collapse probability distribution, i.e. the fragility curve of each frame, with the rate of exceedance for each spectral acceleration and site of interest. The results of this calculation are listed in Table 3.

A trend showing reduced seismic collapse risk with distance from the fault is obvious from the results of Table 3. When the site-to-source distance is decreased from 15 to 10 km the probability of the frames collapsing in 50 years is increased by a factor varying from 1.8 to 1.9 at both the midfault and end-of-fault sites. In addition, collapse risk of the frames located 5 km away from the fault, is 4.0 to 5.0 and 4.7 to 5.0 larger than that when they are located 15 km from the fault, at the midfault and end-of-fault sites, respectively. The aforementioned observations suggest a very large increase in the collapse risk of the structures due to near-fault directivity, even in the case of site-to-source distances of 10 km. In general, modern seismic design codes, such as EC8 [12], use spectra derived from far-field ground motions, the majority of them are recorded at sites with distances from the nearest fault greater than 15 km. Therefore, structures designed based on EC8 [12], which does not take into account near-fault directivity, are more susceptible to collapse, when located at sites close to the fault, since their collapse risk is much larger in this region. Thus, there is a need of introducing in EC8 [12] more strict criteria for the design of structures situated in the near-source.

When comparing the collapse risk at each of midfault and end-of-fault sites for a particular frame, it is observed that the seismic risk is not as largely affected by the relative position of the site to the fault axis as it is by the distance to the fault. However, slightly larger values of the probability of collapse of the frames are found at the end-of-fault sites.
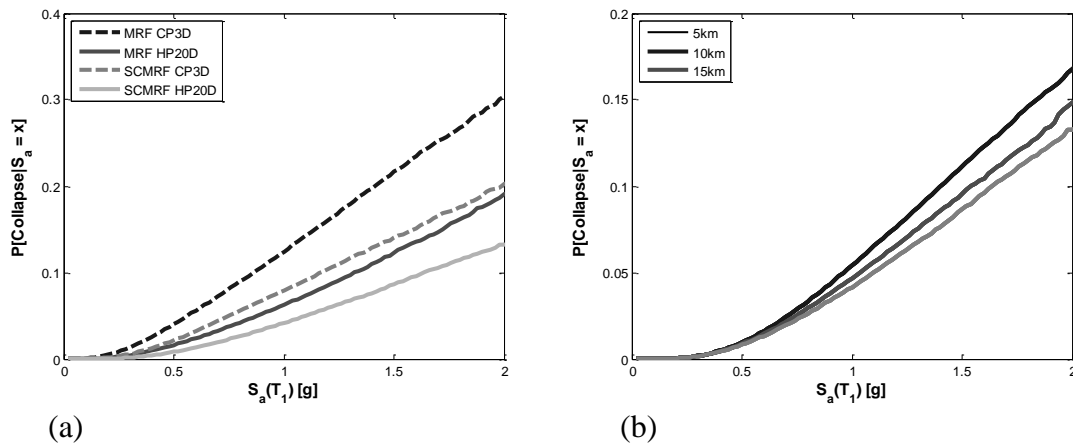
(a)　　　　　　　　　　　　　　　(b)

Figure 7: Collapse fragility functions for (a) all the frames of the study when located at midfault sites for site-to-source distance equal to 15 km (b) the *HP20D* SC-MRF at three different midfault sites.

The efficiency of the SC-MRFs with and without viscous dampers to reduce seismic collapse risk should be evaluated in comparison to the corresponding conventional MRFs. The probability of collapse in 50 years of the *HP20D* SC-MRF is approximately 0.7 times the one of the *HP20D* MRF, for all site-to-source distances and type of sites. A similar trend is observed for the *CP3D* SC-MRF and the *CP3D* MRF. These results indicate that self-centering connections can significantly improve the collapse resistance of the frames. Moreover, self-centering connections are very effective in reducing the collapse risk of the frames to which they were inserted, since an approximately 30% decrease in the collapse risk was observed.

| | P[Collapse in 50 yrs] | | | | | |
| | Midfault sites | | | End-of-fault sites | | |
Frame	5km	10km	15km	5km	10km	15km
HP20D MRF	3.49%	1.40%	0.73%	3.59%	1.46%	0.77%
CP3D MRF	7.36%	3.30%	1.83%	7.55%	3.42%	1.92%
HP20D SC-MRF	2.40%	0.93%	0.47%	2.52%	0.99%	0.51%
CP3D SC-MRF	4.98%	2.14%	1.16%	5.21%	2.28%	1.25%

Table 3: Probability of collapse in 50 years for the frames of this study.

Finally, the effectiveness of providing supplemental damping in the frames examined herein, is investigated. The *HP20D* MRF exhibits 0.5, 0.4 and 0.4 times the probability of collapse in 50 years of the *CP3D* MRF for site-to-source distances equal to 5, 10 and 15 km, respectively, at the midfault sites. Similarly, the *HP20D* SC-MRF has 0.5, 0.4 and 0.4 times the collapse risk of the *CP3D* SC-MRF for site-to-source distances equal to 5, 10 and 15 km, respectively, at the midfault sites. Similar results were obtained at the end-of-fault sites. This suggests that the frames with viscous dampers have superior collapse resistance compared to the frames without viscous dampers. In addition, it can be concluded that supplemental damping reduced the collapse risk of the frames up to 60%, and its effectiveness was increased for larger distances from the fault.

9 CONCLUSIONS

In this paper, the collapse risk of self-centering steel MRFs with viscous dampers subjected to near-fault ground motions was evaluated. The evaluation was based on the comparison of four different designs of a prototype steel building using as lateral load resisting frames: 1) conventional steel MRFs, 2) steel MRFs with viscous dampers, 3) steel SC-MRFs and 4) steel SC-MRFs with viscous dampers. Collapse capacity of these frames was predicted based on the concept of IDA. Results of IDA were combined with NS-PSHA to construct fragility curves for the probability of collapse of the frames and to compute the corresponding probabilities in 50 years. On the basis of the developments presented in this paper, the following conclusions can be drawn:

- The collapse capacity of all the frames strongly depends on the pulse period, T_p, of the excitation and it takes its larger value when the fundamental period of the frames is approximately equal to T_p.

- Collapse risk of the frames is reduced with distance from the fault, indicating that structures designed based on EC8 can be very vulnerable when located in the near source.

- Self-centering connections can significantly improve the collapse resistance of the frames. Moreover, they are very effective in reducing the probability of collapse of the frames to which they were inserted, since an approximately 30% decrease in the collapse risk of all SC-MRFs was observed.

- The frames with viscous dampers have superior collapse resistance compared to the frames without viscous dampers. Supplemental damping is very efficient in reducing the collapse risk of the frames, since an up to 60% decrease was observed, and its effectiveness was increased for larger distances from the fault.

10 ACKNOWLEDGEMENTS

REFERENCES

[1] P.G. Somerville, N.F. Smith, R.W. Graves, N.A. Abrahamson, Modification of Empirical Strong Ground Motion Attenuation Relations to Include the Amplitude and Duration Effects of Rupture Directivity. *Seismological Research Letters*, **68**, 199–222, 1997.

[2] I. Iervolino, C.A. Cornell, Probability of Occurrence of Velocity Pulses in Near-Source Ground Motions. *Bulletin of the Seismological Society of America*, **98**, 2262–2277, 2008.

[3] A. Veletsos, N.M. Newmark, Effect of inelastic behaviour on response of simple systems to earthquake motions. *Proc., 2nd World Conf. on Earthquake Engineering Vol. II*, Tokyo, 895–912, 1960.

[4] V.V. Bertero, S.A. Mahin, R.A. Herrera, Aseismic design implications of near-fault San Fernando earthquake records. *Earthquake Engineering and Structural Dynamics*, **6**, 31–42, 1978.

[5] A.K. Chopra, C. Chintanapakdee, Comparing response of SDF systems to near-fault and far-fault earthquake motions in the context of spectral regions. *Earthquake Engineering and Structural Dynamics*, **30**, 1769–1789, 2003.

[6] G.P. Mavroeidis, G. Dong, A.S. Papageorgiou, Near-fault ground motions and the response of elastic and inelastic, single-degree-of-freedom (SDOF) systems. *Earthquake Engineering and Structural Dynamics*, **33**, 1023–1049, 2004.

[7] B. Alavi, H. Krawinkler, Behavior of moment-resisting frame structures subjected to near-fault ground motions. *Earthquake Engineering and Structural Dynamics*, **33**, 687–706, 2004.

[8] N. Makris, T. Psychogios, Dimensional response analysis of yielding structures with first-mode dominated response. *Earthquake Engineering and Structural Dynamics*, **35**, 1202–1224, 2006.

[9] T.L. Karavasilis, N. Makris, N. Bazeos, D.E. Beskos, Dimensional response analysis of multistory regular steel MRF subjected to pulselike earthquake ground motions. *Journal of Structural Engineering*, **136**, 921–932, 2010.

[10] N. Luco, B.R. Ellingwood, R.O. Hamburger, *Risk-Targeted versus Current Seismic Design Maps for the Conterminous United States*, SEAOC 2007 Convention Proceedings, 2007.

[11] C. Champion, A. Liel, The effect of near-fault directivity on building seismic collapse risk. *Earthquake Engineering and Structural Dynamics*, **41**, 1391–1409, 2012.

[12] EC8. *Eurocode 8. Design of structures for earthquake resistance*, 2013.

[13] J.M. Ricles, R. Sause, M.M. Garlock, C. Zhao, Postensioned seismic-resistant connections for steel frames. *ASCE Journal of Structural Engineering*, **127**, 113–121, 2001.

[14] C. Christopoulos, A. Filiatrault, C-M. Uang, Post-tensioned energy dissipating connections for moment resisting steel frames. *ASCE Journal of Structural Engineering*, **128**, 1111–1120, 2002.

[15] G. Vasdravellis, T.L. Karavasilis, B. Uy, Large-scale experimental validation of steel post-tensioned connections with web hourglass pins. *Journal of Structural Engineering (ASCE)*, **139**,1033-1042, 2013.

[16] C.C. Chou, Y.J. Lai, Post-tensioned self-centering moment connections with beam bottom flange energy dissipators. *Journal of Constructional Steel Research*, **65**,1931-1941, 2009.

[17] C-C. Chou, K-C. Tsai, W-C. Yang, Self-centering steel connections with steel bars and a discontinuous composite slab. *Earthquake Engineering and Structural Dynamics*, **38**, 403-422, 2009.

[18] G. Vasdravellis, T.L. Karavasilis, B. Uy, Finite element models and cyclic behaviour of self-centering post-tensioned connections with web hourglass pins. *Engineering Structures*, **52**, 1-16, 2013.

[19] A. Dimopoulos, T.L. Karavasilis, G. Vasdravellis, B. Uy, Seismic design, modelling and assessment of self-centering steel frames using post-tensioned connections with web hourglass shape pins. *Bulletin of Earthquake Engineering*, **11**, 1797-1816, 2013.

[20] P. Rojas, J.M. Ricles, R. Sause, Seismic performance of post-tensioned steel moment resisting frames with friction devices. *Journal of Structural Engineering*, **131**, 529-540, 2004.

[21] H.J. Kim, C. Christopoulos, Friction damped posttensioned self-centering steel moment-resisting frames. *Journal of Structural Engineering*, **134**, 1768-1779, 2008.

[22] K.C. Tsai, C.C. Chou, C.L. Lin, P.C. Chen, S.J. Jhang, Seismic self-centering steel beam-to-column moment connections using bolted friction devices. *Earthquake Engineering and Structural Dynamics*, **37**, 627-645, 2008.

[23] M. Wolski, J.M. Ricles, R. Sause, Experimental study of a self-centering beam-column connection with bottom flange friction device. *Journal of Structural Engineering*, **135**,479-488, 2009.

[24] M. Garlock, R. Sause, J.M. Ricles, Behavior and design of posttensioned steel frame systems. *Journal of Structural Engineering*, **133**, 389-399, 2007.

[25] H.J. Kim, C. Christopoulos, Seismic design procedure and seismic response of post-tensioned self-centering steel frames. *Earthquake Engineering and Structural Dynamics*, **38**, 355-376, 2008.

[26] T.L. Karavasilis, R. Sause, J.M. Ricles, Seismic design and evaluation of steel MRFs with compressed elastomer dampers. *Earthquake Engineering and Structural Dynamics*, **41**, 411-429, 2012.

[27] T.L. Karavasilis, J.M. Ricles, R. Sause, C. Chen, Experimental evaluation of the seismic performance of steel MRFs with compressed elastomer dampers using large-scale real-time hybrid simulation. *Engineering Structures*, **33**, 1859-1869, 2011.

[28] T.L. Karavasilis, C-Y. Seo, Seismic structural and non-structural performance evaluation of highly damped self-centering and conventional systems. *Engineering Structures*, **33**, 2248-2258, 2011.

[29] C-Y. Seo, T.L. Karavasilis, J.M. Ricles, R. Sause, Seismic performance and probabilistic collapse resistance assessment of steel moment resisting frames with fluid viscous dampers. *Earthquake Engineering and Structural Dynamics*, **43**, 2135-2144, 2014.

[30] Y.C. Kurama, Seismic design of unbonded post-tensioned precast concrete walls with supplementary viscous damping. *ACI Structural Journal*, **97**, 648–658, 2000.

[31] W.Y. Kam, S. Pampanin, A. Palermo, AJ. Car, Self-centering structural systems with combination of hysteretic and viscous energy dissipations. *Earthquake Engineering and Structural Dynamics*, **39**, 1083-1108, 2010.

[32] A.S. Tzimas, A.I. Dimopoulos, T.L. Karavasilis, EC8-based seismic design and assessment of self-centering steel frames with viscous dampers. *Journal of Constructional Steel Research*, **105**, 60-73, 2015.

[33] S. Mazzoni, F. McKenna, M. Scott, G. Fenves, *Open system for earthquake engineering simulation (OpenSees). User Command Language Manual*, Pacific Earthquake Engineering Research Center, University of California, Berkeley, 2006.

[34] D. Vamvatsikos, C.A. Cornell, Incremental dynamic analysis. *Earthquake Engineering Structural Dynamics*, **31**, 491-514,2002.

[35] D.G. Lignos, H. Krawinkler. Deterioration Modeling of Steel Components in Support of Collapse Prediction of Steel Moment Frames under Earthquake Loading. *Journal of Structural Engineering*, **137**, 1291-1302, 2011.

[36] M. Hamidia, A. Filiatrault, A. Aref, Simplified seismic sidesway collapse analysis of frame buildings. *Earthquake Engineering and Structural Dynamics*, **43**, 429–448, 2014.

[37] T.L. Karavasilis, A.I. Dimopoulos, A.S. Tzimas, George S. Kamaris, D. Vamvatsikos, estimation of economic losses in seismic-resistant post-tensioned steel frames with viscous dampers, 8th *International Conference on Advances in Steel Structures (ICASS 2015)*, Lisbon, Portugal, July 22-24, 2015.

[38] H. Krawinkler, Shear Design of Steel Frame Joints. *Engineering Journal*, AISC, **15**, 82-91, 1978.

[39] J.W. Baker, Quantitative Classification of Near-Fault Ground Motions Using Wavelet Analysis. *Bulletin of the Seismological Society of America*, **97**, 1486–1501, 2007.

[40] Pacific Earthquake Engineering Research Center (PEER), NGA Database. http://peer.berkeley.edu/nga/.

[41] FEMA P695, *Quantification of building seismic performance factors*. ATC-63 Project. Applied Technology Council. CA. USA; 2008.

[42] A.B. Liel, C.B. Haselton, G.G. Deierlein, J.W. Baker, Incorporating Modeling Uncertainties in the Assessment of Seismic Collapse Risk of Buildings. *Structural Safety*, **31**, 197–211, 2009.

[43] J.W. Baker, C.A. Cornell, Spectral shape, epsilon and record selection. *Earthquake Engineering and Structural Dynamics*, **35**, 1077−1095, 2006.

[44] C.B. Haselton, J.W. Baker, A.B. Liel, G.G. Deierlein, Accounting for Ground Motion Spectral Shape Characteristics in Structural Collapse Assessment Through an Adjustment for Epsilon. *Journal of Structural Engineering*, **137**, 332–344, 2011.

[45] P. Tothong, C.A. Cornell, J.W. Baker, Explicit Directivity-Pulse Inclusion in Probabilistic Seismic Hazard Analysis. *Earthquake Spectra*, **23**, 867–891, 2007.

[46] S.K. Shahi, J.W. Baker, An Empirically Calibrated Framework for Including the Effects of Near Fault Directivity in Probabilistic Seismic Hazard Analysis. *Bulletin of the Seismological Society of America*, **101**, 742–755, 2011.

[47] E. Chioccarelli, I. Iervolino, Near-Source Seismic Demand and Pulse-Like Records: a Discussion for L'Aquila Earthquake. *Earthquake Engineering and Structural Dynamics*, **39**, 1039–1062, 2010.

[48] E. Chioccarelli, I. Iervolino, Near-source seismic hazard and design scenarios. *Earthquake Engineering and Structural Dynamics*, **42**, 603-622, 2013.

[49] E. Chioccarelli, I. Iervolino, Sensitivity analysis of directivity effects on PSHA. *Bollettino di Geofisica Teorica e Applicata*, **55**, 41-53,2014.

[50] PG. Somerville, Magnitude Scaling of the Near Fault Rupture Directivity Pulse. *Physics of the Earth and Planetary Interiors*, **137**, 201–212, 2003.

[51] D.L. Wells, K.J. Coppersmith, New empirical relationships among magnitude, rupture length, rupture width, rupture area, and surface displacement. *Bulletin of the Seismological Society of America*, **84**, 974-1002,1994.